universität wien

MASTERARBEIT | MASTER'S THESIS

Titel | Title

In-situ Measurement of the α-to-β Transition in Human Hair under Varying Conditions

verfasst von | submitted by

Johannes Liebhart BSc

angestrebter akademischer Grad | in partial fulfilment of the requirements for the degree of

Master of Science (MSc)

Wien | Vienna, 2025

Studienkennzahl lt. Studienblatt | Degree programme code as it appears on the student record sheet:	UA 066 876
Studienrichtung lt. Studienblatt | Degree programme as it appears on the student record sheet:	Masterstudium Physics
Betreut von | Supervisor:	Univ.-Prof. Mag. Dr. Herwig Peterlik

Acknowledgements

First of all, I would like to thank my supervisor Univ.-Prof. Dr. Herwig Peterlik for giving me the opportunity to work on this thesis and for guiding me throughout the process. His valuable advice was always helpful and available when needed.

Next, I would like to thank Martin Haßler for his support and explanations during the project, as well as for his help in proofreading through the work. Additionally, I would like to thank him for providing his hair as sample material.

A special thanks goes to my family for their unrestricted support during my studies. Especially my parents and grandmother helped me a lot, whenever I needed them.

I am especially grateful to my girlfriend, Cindy, whose encouragement and motivation played a crucial role in the final months of my Master's degree.

Last but not least I also want to thank my best friends, Christoph and Bernhard, for their emotional support and motivation throughout my whole studies. Without you it would have been a very hard time.

Thank you all very much!

Contents

1. Introduction

Hair is omnipresent in today's society. It is not only a part of our bodies, but also a symbol of beauty, body care, lifestyle and health. Many people spend a lot of money on various hair care products to achieve the desired shape or color. But to keep long hair healthy for longer and prevent it from breaking or falling out, many products are used. It is therefore important to understand how hair is structured and how it behaves under different conditions and stresses.

1.1. Experimental Motivation and Setup Differences

The basis of this thesis is the work of Kreplak et al. [1], where the so-called $\alpha - \beta$ transition in horse hair could be observed in a synchrotron radiation source with exposing hair to steam, i.e. heavy environmental conditions. The experimental evidence was a change in the X-ray pattern, where the disappearance of X-ray peaks as well as the occurrence of new intensity maxima was attributed to a structural change of the secondary protein structure, the transition from α-helices to β-pleated sheets. This led us to three questions:

1. How extreme conditions are required to trigger the transition – is steam necessary or are humid conditions sufficient?

2. Is there a humidity or strain threshold, above which a transition takes place?

3. Is a synchrotron radiation source essential or can this transition be also observed in a conventional laboratory X-ray equipment?

To answer these questions, an in-situ tension test equipment was used to follow the development of the X-ray patterns under load. This tension test equipment works in an environment with the possibility to vary humidity and temperature conditions. The equipment is described in section 3 and the experimental results in section 4. A discussion of the limitations follows in section 5.

1.2. Literature overview

In this section an overview of used literature as well as results from previous studies is given. The foundation of research on the detection and investigation of the α-to-β transition was made by the work of Astbury et al. [2], who first used X-ray diffraction methods to study the molecular structure of keratin fibers in wool and hair. As a result they found, that keratin primarily exists in a helical structure, called the α-helix. But under extension it can undergo a structural transformation, which leads to a β-sheet arrangement. Their work was limited by the possibilities of the time but later studies expanded upon this foundation.

The central literature used as a basis for this thesis, which is also built on the foundation of Astbury, are the two studies of Kreplak et al. [1, 3]. They showed the α-to-β transition in horse hair under mechanical stress at a synchrotron light source. The exposure of the samples to steam led to changes in the X-ray diffraction pattern, with some peaks vanishing and new ones emerging.

Another synchrotron study focused on the effect of mechanical deformation in human hair and wool. The investigations of Cao et al. [4] revealed that the α-to-β transition is related to mechanical deformation. The structural change of the keratin shows similar characteristics as polymers due to the effect of a "necking" deformation. This results in necked zones which prefer the β-sheet structure and other zones remaining in α-helical configuration.

A very different but equally important study is that of Minin et al. [5], where they measured the α-helix to β-sheet transition in polypeptide coiled coils. Although that study is about proteins in general, it offers context and understanding for observations of the α-to-β transition in keratin. One of their key insights is that α-helices first elongate and partially unfold before rearranging into β-sheet structures, supporting experimental observations that mechanical stretching is needed for the transition. Additionally, they showed that hydration and environmental factors significantly influence the structural stability of α-helices.

The study of Lyman et al. [6] shows the influence of temperature variations of the water used to wet the horse hair samples. These changes to the environmental factor lead to different orientations of the β-sheets (parallel and anti-parallel). As one of the measurements in their research was performed with 21 °C warm water, this could give the possibility of measuring the α-to-β transition at room temperature and humid conditions.

In the study of Yu et al. [7] the focus was on the deformation processes of human hair. An important finding was that keratin exhibits viscoelastic behavior, meaning that both

the rate and magnitude of stress influence the structural transformation. In addition, they observed that the mechanical response varies depending on whether the conditions are dry or humid.

Furthermore, the study by Stanić et al. [8] used a setup with a sub-micron X-ray beam at a synchrotron to be able to measure different regions of a single hair fiber. As a result, they showed that the hair has different local structures with the cuticle containing β-sheets.

In summary most prior studies are demonstrating the α-to-β transition using a synchrotron radiation source. A key objective of this thesis is to test if this structural change can also be investigated using a laboratory based small-angle X-ray scattering (SAXS) setup. Most of the previous studies exposed the samples to steam, but this work should show if high humidity in combination with mechanical deformation is sufficient to trigger the transition.

2. Theoretical background

This chapter explains the theory behind the structure of human hair, an overview of the properties that were measured in the theses and the used measuring technique.

2.1. X-ray Scattering

For the measurements in this thesis the method of choice is wide angle X-ray Scattering (WAXS). The basic principles of this technique are described in this section.

2.1.1. X-rays

Wilhelm Conrad Röntgen discovered X-rays in 1895. Their wavelength ($10^{-8} - 10^{-11}$ m) is comparable to the interatomic distances of ~ 1 Å and between gamma rays and ultraviolet light (see fig 2.1). [9, pp. 237–238]

For the generation of X-rays, for technical use, there are a couple of possible sources. Typically these can be synchrotrons or X-ray tubes. Both of them generate the X-rays via the emission of radiation, caused by accelerated charges. However they differ in intensity, brilliance and accessibility in a typical lab.

A synchrotron is a large experimental facility - a special type of particle accelerator. For the generation of X-rays in a synchrotron usually electrons are accelerated to relativistic velocities and forced on a circular path. As the electrons are bent to their ring shaped path by magnets, they lose energy. This loss is then emitted as in form of synchrotron radiation, which is a continuous spectrum of Bremsstrahlung [1] in the wavelength range of X-rays. Because it produces a continuous spectrum, this type of source is useful for a lot of different projects and applications, as it can be tuned and or filtered by suited optics. A synchrotron also produces a highly intense beam, enabling experiments with weakly scattering samples, which would not be possible with other sources. The disadvantages of these facilities are that they are very cost intensive and large. Therefore only a few of them exist worldwide and measuring time is valuable. Summarizing, synchrotrons are

[1] a German word that can be translated either with "braking radiation" or "deceleration radiation"

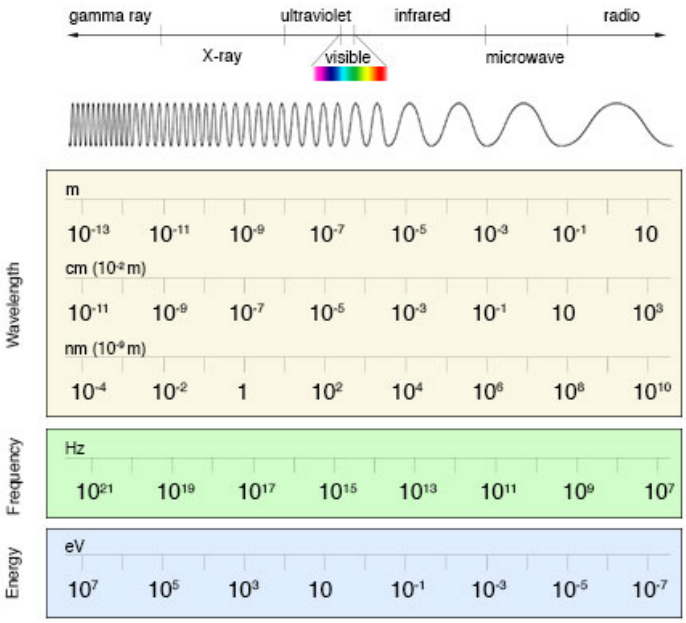

Figure 2.1.: Overview of the wavelengths, frequencies and energies of the electromagnetic spectrum. Image credit: NASA's Imagine the Universe (NASA/GSFC) [10].

the primary choice if small beams, high brilliance, energy tunability and large coherence lengths are required for experiments. [11, pp. 38–39]

A X-ray tube is a small, compact device that can be installed in a regular lab and is much less cost intensive than a synchrotron. Therefore these are very easily accessible. Thus experiments can be easily prepared and repeated, if something fails. A scheme of a basic X-ray tube is shown in figure 2.2. A filament, which is typically made of tungsten, acts as the cathode. Electrons are emitted from the filament and accelerated to the anode by a high voltage. The system used in this work uses a copper X-ray source, i.e. the anode is made of copper. Due to the bombardment of the electrons on the anode, which mainly produces phonons and therefore heat, the system requires a form of cooling. The electrons that are colliding with the anode material are decelerating by one or multiple collisions. Each of those collisions decreases the energy of the electron by ΔE until the electron is at rest.[2] The energy loss is turned into X-ray radiation with the wavelength determined by the energy difference $\Delta E = \frac{hc}{\lambda}$. As the losses can vary, the resulting X-ray spectrum is a continuous spectrum with a maximum energy determined by the accelerating voltage. The typical spectrum of such a X-ray tube is shown in figure 2.3. In the figure one can

[2]So it also generates a broad spectrum of X-rays via Bremsstrahlung.

see that the spectrum starts at zero at a small wavelength, which marks the maximum possible energy of the emitted photons and depends on the accelerating voltage of the X-ray tube. This maximum possible energy is caused by one electron losing all kinetic energy in one singular collision. Looking at the spectrum again, also shows two very prominent peaks labeled as K_α and K_β. These element specific X-ray lines and are caused by electron transitions in the target atom. An incident electron with enough energy can eject an electron of the K-shell of the atom. The required energy to achieve this is defined as the work function W_K, where the K stands for the K-shell. Following this, an electron from an energetic higher level transitions to fill the vacancy. This is accompanied by the emission of an X-ray photon with an energy depending of the origin of the transition electron. If the electron transitions from the L-shell to the K-shell, the radiation is called K_α and if it is from the M-shell to the K-shell, it is called K_β. In order to get rid of the unwanted K_β line, a X-ray filter with a high absorbance for wavelengths smaller than K_α is used (see figure 2.3). But as the L-shell has three energy levels, electrons from either of these levels can transition, which results an three closely separated wavelengths, denoted by an additional index 1,2 or 3. Hereby is the intensity of the $K_{\alpha1}$ the highest, $K_{\alpha2}$ about half as intense and $K_{\alpha3}$ very weak. For high resolution measurements, one wants to have only the $K_{\alpha1}$ line. As a result a special crystal monochromator is needed, that can only reflect the particular wavelength of $K_{\alpha1}$. For a copper X-ray tube this wavelength is $K_{\alpha1} = 1.5406\,\text{Å}$. For high intensity measurements both the $K_{\alpha1}$ and $K_{\alpha2}$ line are used, as this requires less optical elements and thus less losses. [9, pp. 237–240]

The disadvantage of rotating anode systems, which deliver a high intensity X-ray beam, is that they have a high power consumption (typically $5 - 18$ kV) and thus require active cooling. The used laboratory setup, has an Incoatec IμS 2.0 X-ray microsource, which uses a focused electron beam to irradiate a small point on the anode. Together with a comparable low wattage of 50 W, this makes it possible to operate it without water cooling of the tube. The emitted wavelength is filtered differently, as a mirror setup that only allows $K_{\alpha1}$ loses a lot of intensity. To mitigate this, a Montel optics system is built in. These optics consist of multiple mirrors, which are shaping the beam in two dimensions. This helps with collimating the beam, ensures a high brightness and symmetrical beam. Although the beam does use a mixture of both $K_{\alpha1}$ and $K_{\alpha2}$ it still has a high spectral purity, with a weighted mean wavelength of $\lambda = 1.5418\,\text{Å}$. [12] [11, p. 35]

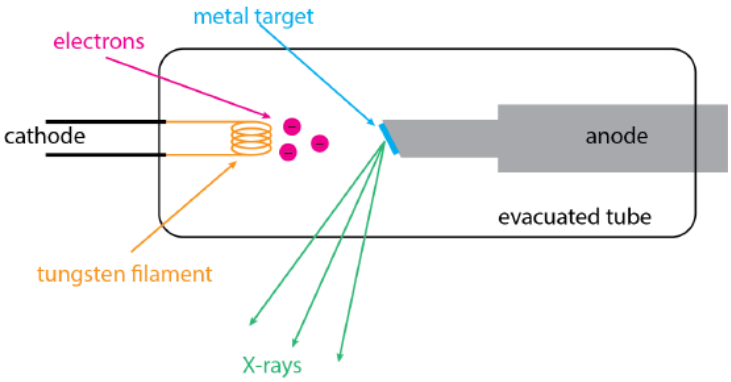

Figure 2.2.: Schematic design of a X-ray tube. Image credit: David Harvey, LibreTexts Chemistry. Licensed under CC BY-NC-SA 4.0 [13].

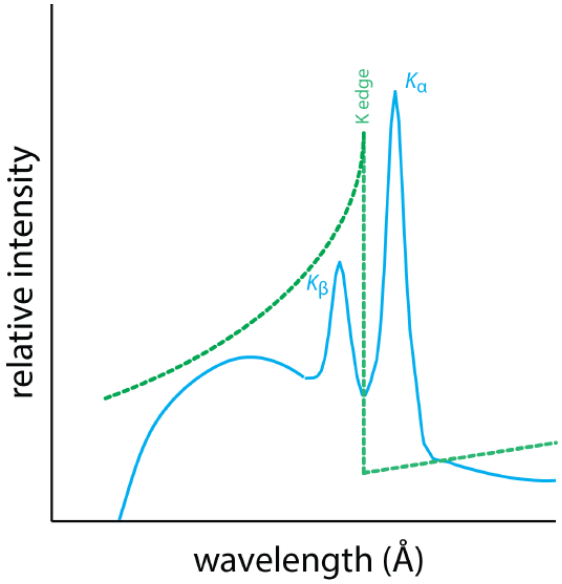

Figure 2.3.: X-ray emission spectrum (blue) with the characteristic peaks K_α and K_β and the absorbance spectrum of a X-ray filter (green). Image credit: David Harvey, LibreTexts Chemistry. Licensed under CC BY-NC-SA 4.0 [13].

2.1.2. Principles of Scattering

In the previous section the characteristics and generation of the used radiation for the experiments was explained. This section contains the foundation of how X-rays interact with the matter of the sample and how the resulting image is formed. Most of the information in this section is based on the books "Introduction to Solid State Physics" by Charles Kittel [14, pp. 25–32, 39–43], "Festkörperphysik" by Rudolf Gross and Achim Marx [15, pp. 67–83] and the "SAXS-Guide" by Schnablegger and Singh [11, pp. 16–22].

The scattering theory explains how waves (in this case X-rays) interact with matter. The incident wave can either be scattered or absorbed by the molecules or atoms in the target. From the scattered waves various information about the structure of the material can be obtained. The scattering process can be categorized into two types. One is elastic scattering, where the energy of the scattered wave is conserved and the other is inelastic scattering, where an energy transfer between wave and material takes place.

Inelastic Scattering

As mentioned before, inelastic scattering involves a transfer of energy between the photon and the electron. This results in a change of the wavelength of the photon and is called Compton scattering. The photon gives a part of its energy to the electron. As there is no particular phase relationship with the incident wave, there cannot occur any interference. Therefore this type of scattering only contributes to the background and does not provide any information about the structure of the material.[11, p. 16]

Elastic Scattering

Elastic scattering is the fundamental basis for measuring the structural quantities of materials using WAXS. This scattering process does not have an energy exchange between the photon and the target, but the photon changes its direction due to the interaction. The process is also called Thomson scattering. To be able to explain the diffraction process of waves a few things need to be introduced and derived. First we consider that a plane wave hits on a Bravais lattice. The plane wave has the mathematical form of:

$$\Psi(r) = \Psi_0 \exp\left(i\vec{k} \cdot \vec{r}\right) \tag{2.1}$$

where Ψ_0 is the amplitude of the wave, $\vec{r}$ is the position vector in real space and $\vec{k}$ is the wave vector that describes the direction of motion of the wave. The wave vector is related to the wavelength λ by $\left|\vec{k}\right| = \frac{2\pi}{\lambda}$. As this is the elastic case, the energy and

magnitude of the wave vector is conserved and only the direction of the scattered wave vector is different from the incident one, as shown in figure 2.4, meaning $\left|\vec{k_i}\right| = \left|\vec{k_s}\right|$. In the figure one can also see, that the difference of the scattered and incident vector gives the reciprocal vector $\vec{G}$ or the scattering vector $\vec{q}$:

$$\vec{G} = \vec{k_s} - \vec{k_i} = \vec{q} \tag{2.2}$$

A simpler and more practical representation of the Laue condition in equation 2.2 is Bragg's Law, which is written as:

$$n\lambda = 2d\sin\theta \tag{2.3}$$

where n is the order of diffraction, λ is the wavelength of the incident X-rays, d is the spacing between atomic planes in the crystal, and θ is the angle of incidence relative to the lattice planes. Bragg's Law describes how the phase difference between waves scattered from successive atomic planes leads to constructive interference when the path difference $2d\sin\theta$ is an integer multiple of the wavelength.

From figure 2.4 one directly obtains, that $q/2 = k\sin\theta$ and with $\left|\vec{k}\right| = \frac{2\pi}{\lambda}$ this gives:

$$q = \frac{4\pi\sin\theta}{\lambda} \tag{2.4}$$

The formula shows that q and 2θ are proportional in the approximation of small angles $\sin\theta \approx \theta$, but for larger angles this approximation does not hold and becomes nonlinear. However, a larger q-value still gives a larger scattering angle. It is proportional to $1/\lambda$, which sets the dimension of q as m^{-1} (q is a vector in the reciprocal space). Understanding how the q-values, which are obtained from analyzing the scattering images, are related to the real space and scattering angles, is very important. The visible pattern in the scattering images are a result of interference of the scattered waves and the incoming beam, as all of these waves are coherent because of the elastic scattering.

Atomic Form Factor

To take into account that different types of atoms have different electron densities, which impacts the ability to scatter a photon, the atomic form factor $f(\vec{q})$ is needed. It quantifies how the scattering amplitude changes as a function of the scattering vector $\vec{q}$. The formula is defined as:

$$f(\vec{q}) = \int \rho(\vec{r})\exp(i\vec{q}\cdot\vec{r})d\vec{r} \tag{2.5}$$

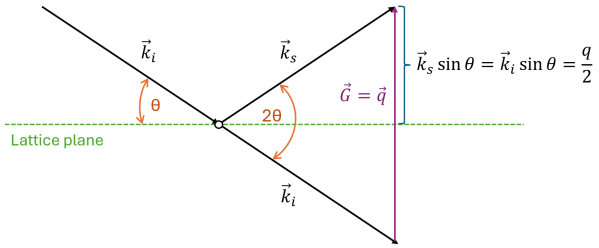

Figure 2.4.: Scheme for the derivation of the Bragg law from the Laue condition. With the incoming wave with wave vector $\vec{k_i}$, the scattered wave vector $\vec{k_s}$, scattering vector $\vec{q}$ and scattering angle 2θ.

where $\rho(\vec{r})$ is the electron density at the position $\vec{r}$. As X-rays mostly interact with the electron cloud, elements with a higher atomic number and therefore more electrons have a larger form factor. This leads to a higher scattered intensity.

Structure Factor

In order to describe the total scattering amplitude, which is influenced by all atoms in the unit cell, the structure factor $F(\vec{q})$ is needed. This factor takes the position of the atoms and their corresponding form factor into account. This can be described with the formula:

$$F(\vec{q}) = \sum_{n=0}^{N} f_n \exp(i\vec{q} \cdot \vec{r}_n) \tag{2.6}$$

where f_n is the atomic form factor of the n-th atom and $\vec{r_n}$ is the position of the n-th atom in the unit cell. This formula can also be rewritten in Miller indices notation. To write it in terms of Miller indices the position vector is $\vec{r_n} = (x_n, y_n, z_n)$ and $\vec{q} = ha^* + kb^* + lc^*$, where a^*, b^* and c^* are the basis vectors of the reciprocal lattice. This then leads to the formula of the structure factor:

$$F_{hkl} = \sum_{n=0}^{N} f_n \exp[2\pi i(hx_n + ky_n + lz_n)] \tag{2.7}$$

The intensity of the scattering pattern depends on the square of the structure factor:

$$I(\vec{q}) \propto |F_{hkl}|^2 \tag{2.8}$$

For a peak in the scattering pattern the structure factor needs to be non zero. If it is zero, this would result in destructive interference and therefore in no peak. For certain crystal systems these are specific combinations of h, k and l and give so called systematic absences. [9, pp. 203–210]

2.1.3. Calibration of the Detector Distance

In order to know the correct distance from sample to the detector, a measurement with a well known specimen is performed. This are usually some crystals like silver behenate (AgBh) for SAXS measurements or for WAXS aluminum oxide (Al_2O_3). The aluminum oxide has a hexagonal close-packed (hcp) structure. Because of this the resulting diffraction pattern has a certain set of Bragg peaks, which correspond to specific interplanar spacings and the symmetry of the crystal lattice. The atomic planes in the crystal are notated with the Miller indices (hkl). Systematic absences occur due to destructive interference, which arises when the contributions of scattered waves from symmetrically equivalent atoms cancel out. This happens if the structure factor $F(q) = 0$ for a certain set of h, k, l. For the case of a hcp crystal like Al_2O_3 this is true for reflections where $h - k$ is not divisible by 3. As the systematic absences are known, the reflexes for constructive interference and therefore peaks in the diffraction pattern are also known and can be found in tables. These predictable and well-characterized peaks make Al_2O_3 an excellent calibration standard for scattering experiments. By comparing the observed positions of Bragg reflections to their theoretical scattering angles, the detector distance can be precisely calibrated. This ensures the reliability of calculated scattering vectors $\vec{q}$ and subsequent structural analyses. [9, pp. 392-396]

2.1.4. Image plates

Image plates are able to store the energy of the scattered X-rays by exciting electrons into a meta-stable state. Upon exposure to X-rays, electrons in the image plate's phosphor layer are elevated to higher energy levels, creating a latent image. The image plate then has to be read out by a special scanner, which uses a laser that makes the image plate to emit visible fluorescent radiation. The scanner then produces a digital image on the computer, where the intensity in the image is proportional to the amount of absorbed X-ray photons. To reset the image plate for another measurement, it needs to be cleared on a light pad for at least 3 min. The disadvantage of the image plates is that the read out, clearing and putting the plate back in its place for another measurement cannot be automated and therefore needs an operator on site. Another disadvantage is that image

plates have a threshold, which makes an evaluation of weak signals difficult. It is also important to make sure, that the lab room needs to be as dark as possible, as artificial light can excite electrons in the plate or erase some.[11, pp. 45–46][16, pp. 89–91]

2.2. Hair

Hair is a biological tissue that is built as a composition of multiple smaller structures. The hierarchical structure and the typical size of the individual parts are shown in figure 2.5. One can distinguish between two major parts of a hair, the cuticle and the cortex. The cuticle contains the outer layers, which consists of cells that form a scale like structure. The cortex forms the larger part of the hair fiber. [17, pp. 2–3] Keratin is distinguished in two types the α- and β-keratin. Where α-keratin is found in hair, wool, horn, nails and hooves. β-keratin occurs typically in reptiles and birds and is found in hooks or scales. This type of keratin is different from the α-keratin, which is the subject of this thesis and therefore not relevant to go into further detail. However, it is worth to note, that this classification and naming of the two different types of keratin exists, as both of these keratin variants have internal structures (the so called secondary protein structure), which are also called α and β. As this can be very confusing it is important to know that these are two very different things and for the rest of this thesis α and β-keratin only refers to the α-helix and β-sheet secondary structure of the α-keratin protein. [18, pp. 165–168]

2.2.1. α-helix and β-sheet structure

For this thesis the focus is on the structure of the keratin proteins. Proteins can form a few different secondary structures, where the protein chains form regular shaped and repeating segments. The two most common types of these secondary structures are the so called α-helix and β-sheet. In the case of keratin the α-helix is the more prominent form. To form the helix structure, the protein chain is wrapped around an imaginary axis, forming a long spiral. The spiral can either be left-handed or right-handed but in the case of keratin it is a right-handed one. As the helix is a segmented structure, one can determine the size of one segment, which is 0.52 nm long, measured in the longitudinal axis as shown in the figure 2.6. One of those segments contains 3.6 residues, which means that per turn on the spiral there are 3.6 amino acids. [19, pp. 119-122, 126]

The other possible configuration of the keratin is the β-sheet structure. In comparison to the α-helix, the polypeptide chain does not form a spiral but a zigzag pattern. Multiple zigzag strands that are next to another, form the sheet structure. Hereby it

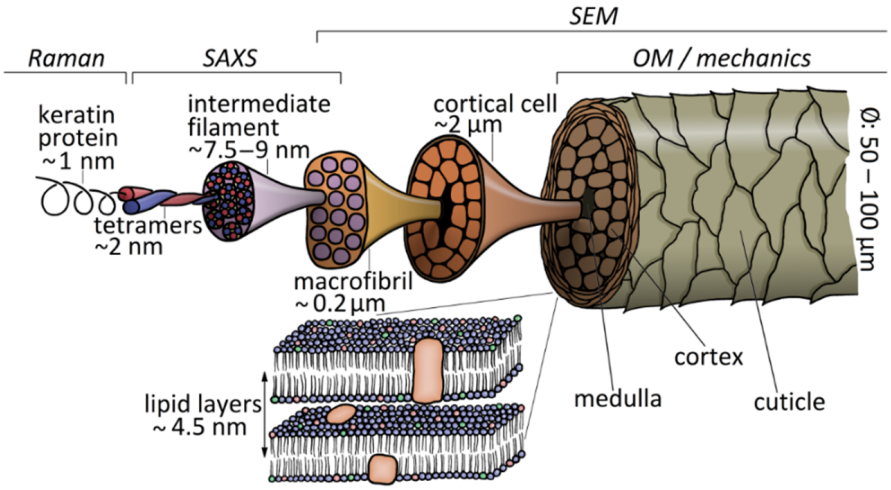

Figure 2.5.: Structural hierarchy of hair. Reused from [20, p. 2].

can be differentiated between a parallel and antiparallel sheet. The difference here is the orientation of the amino-to-carboxyl parts. This means how the two ends of the molecule are located. As a result the hydrogen bonds in the sheet structure are also different. In the antiparallel they are in-line with the sheet, whereas in the parallel configuration they are not. [19, p. 123]

2.2.2. Structures of interest

The most striking proof for a structural transition is a change in the X-ray diffraction pattern. This means that there are some peaks in the spectrum, which are corresponding to structures, that are linked to either the α-helical or β-sheet configuration. The α-to-β transition would then show up in the WAXS image by the fact that with a change in the conditions, peaks caused by α-helices disappear and those peaks of the β-sheets appear. For this thesis the focus was on the following peaks:

1. A peak at 0.52 nm, which corresponds to the periodicity of the α helix. However this peak is superimposed with another one. The second peak is at 0.5 nm and appears from less ordered coiled coils.

2. The peak at 0.333 nm is connected to the distance between residues of the polypeptide chain of the β-sheet structure.

3. The 0.465 nm peak corresponds to the lateral distance between the β-sheets.

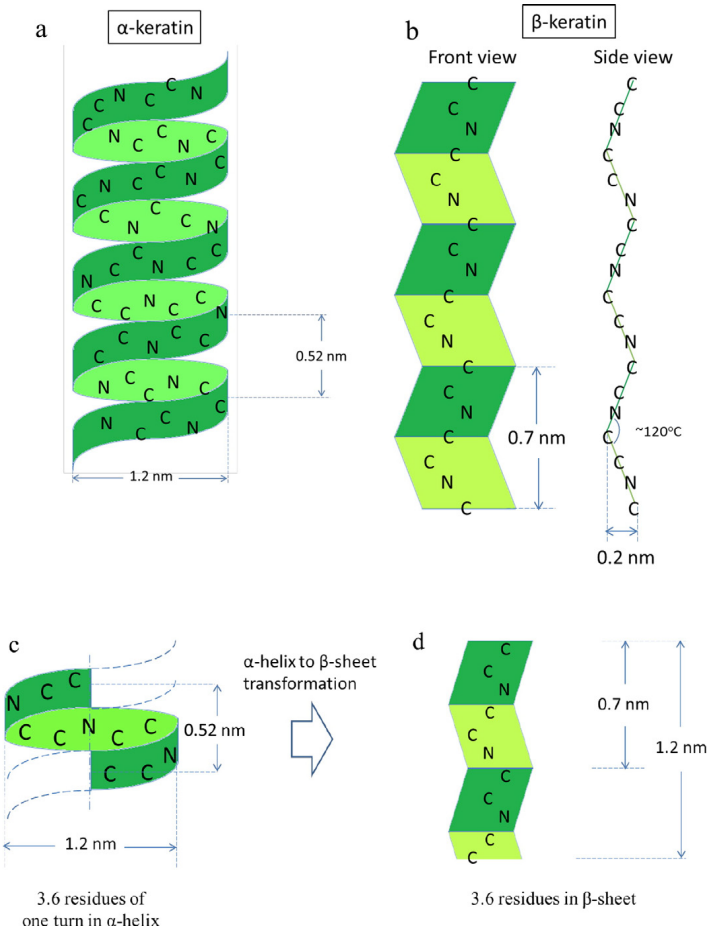

Figure 2.6.: Scheme of the helical structure of the α-keratin and the pleated sheets of the β-keratin. (c) and (d) show that one turn of the helix spiral transforms into 3.6 sheets. Reused from [7, p. 161].

There are two peaks linked to the existence of the β-sheets in the sample and one to an α-helix. The idea is that, because of the α-to-β transition, the 0.52 nm peak vanishes and the other two peaks appear. For the evaluation it is important to note, that the 0.52 nm and 0.333 nm peak are on the meridian axis, so they appear parallel to the orientation of the hair samples. Whereas the 0.465 nm peak is on the equatorial axis and perpendicular to the specimen. [3, p. 640] For the analysis of the data one needs to be careful, as the image plate reader rotates the images by 90° and therefore the pattern looks different than in other literature.

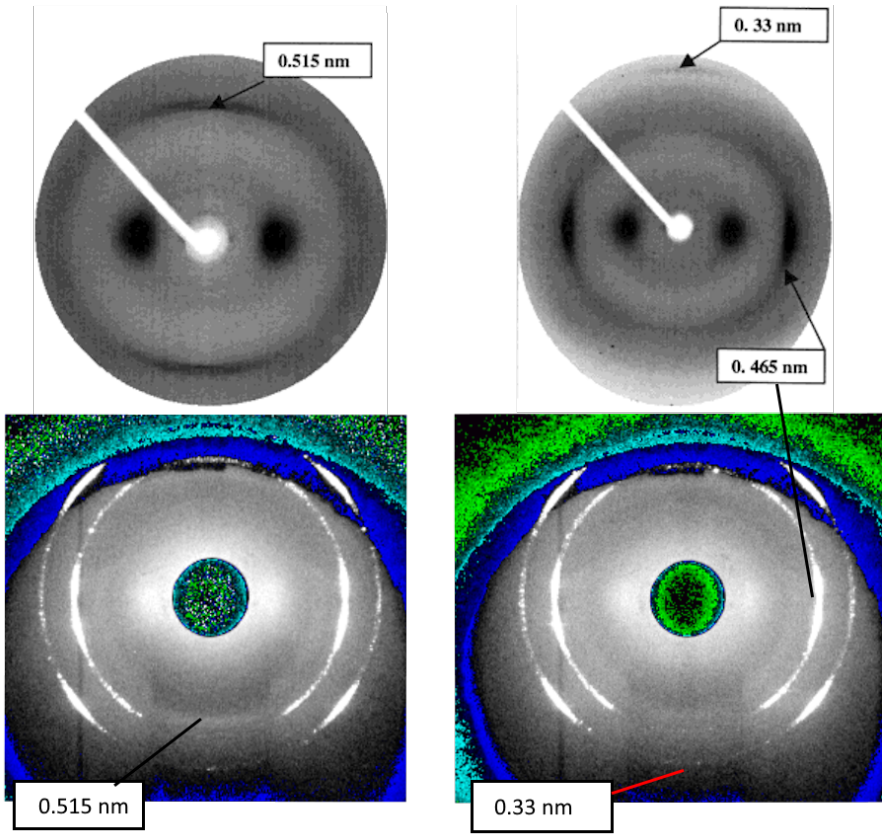

Figure 2.7.: Comparison of the diffraction WAXS images of the measurements of Kreplak (top row, adapted from [1, p. 527]) and the ones in this thesis (bottom row). The top left image shows typical α-keratin, where the peak of 0.515 nm is visible. The bottom left picture is from the measurement at 60% relative humidity and a strain of 10%. There is an indication marker for where the 0.515 nm should be expected in the pattern. The top right image from Kreplak shows the typical pattern of β-keratin, with the two important peaks marked. In the bottom right picture there are also markings for the expected positions of these peaks. This image was recorded at a strain of 40% and 60% relative humidity. The very bright extended spots are caused by the oriented structure of Kapton, from which the window of the sample chamber is made of. The blue and green spots in the picture are due to a different color scale.

3. Materials and Methods

This chapter shows the preparation of the sample material and describes the various machines needed for conducting the experiments as well as the final setup.

3.1. Samples and Preparation

The samples are human hair donated from my colleague Martin Haßler. It is natural straight blonde hair without any chemical treatment. The hair has been stored in a dry environment for about a year before the measurement.

30 hairs are glued to a piece of paper, which serves as a frame, to be able to fit it into the tensile machine correctly. The total length of one of those frames is 20 mm but on the top and bottom of the frame 5 mm are used for fixating the sample. This results in a clamping length of 10 mm. One of the used samples is shown in the figure 3.1. The glue used for the samples was the gel superglue by UHU. A few different glues have been tested for their strength under the experimental conditions. These tests are shown in the section 4.2. After installing the frames in the tensile machine, the paper strips on the side are cut off and the setup is ready for starting a tension test.

3.2. Tensile Machine

The tensile machine used in this thesis is built into a humidity chamber and was already used in a previous thesis from Alexander Müllner. The chamber is made out of aluminum and is leak proof. On the front and the back side there is a circular window, which is covered by regular aluminum foil. These windows, covered by thin foil, are needed to allow the X-rays to pass through the chamber and keeping a stable humidity inside. In comparison to the previously conducted experiments with this apparatus the window on the backside is too small. To visualize larger scattering angles a new plate with a larger diameter windows is needed. Because the whole chamber is also insulated with XPS-material, it is also required to make a new rear panel with a larger hole too.

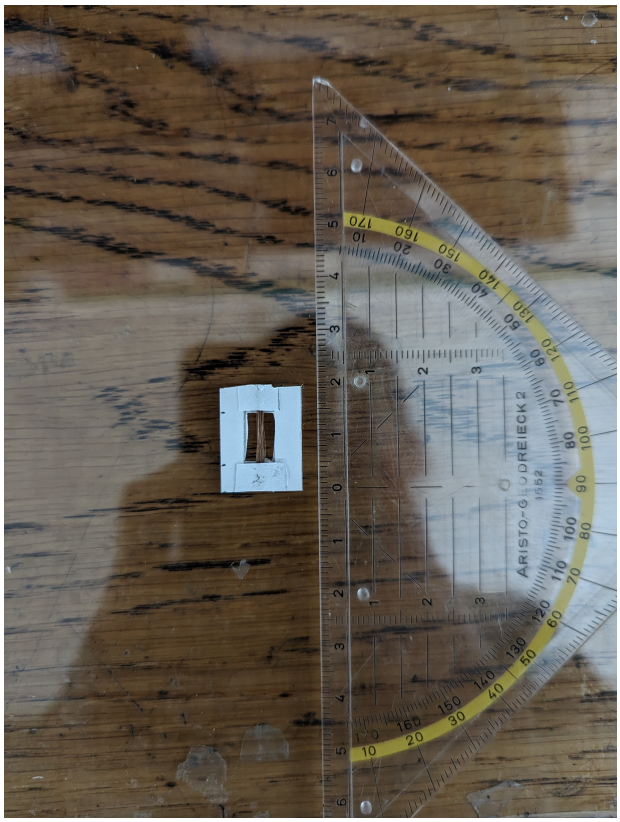

Figure 3.1.: Typical picture of one of the prepared samples.

3.2.1. Humidity Control

To control the temperature and relative humidity for the different steps of the experiment the modular humidity generator MHG32 by ProUmid [21] is used. This machine consists of a controlling unit, where it is possible to set the parameters for the relative humidity and the gas flow, as well as setting the machine on stand-by. In comparison to other humidity generators the MHG32 creates the gas-water mixture not in the controlling unit but near the point of application in a small square shaped mixing chamber, where dry N_2 gas and N_2 gas saturated with water are mixed to the desired value. There are a couple of tubes and cables going into the mixer. In the sample chamber there is also a sensor for temperature and humidity, which gives the MHG32 the information about how the current state of humidity is inside the chamber and if it has to adept the mixing to reach or stay at the given relative humidity. Additionally there is also an circulatory water bath, which is used to control the temperature of the chamber itself. For easier control of the humidity settings, as well as being able to log the change of humidity during the experiment, a program developed by Stephan Puchegger is used.

3.2.2. Tension Control

The sample is clamped with a small block of aluminum and two screws on the top and bottom of the tensile test machine. To increase the friction and prevent possible slipping of the sample under tension, a small piece of sandpaper is glued onto the aluminum. A small motor can move the top crosshead by moving the rod it is fixated on. With a sensor the displacement and the current load can be measured. The tensile test machine is controlled with a EDCi22 by DOLI. With another software provided by Stephan Puchegger, the tensile machine can be controlled and the data of load and displacement are logged into a file.

3.2.3. Testing of different Glues

Before the measurements could begin, the choice of a suitable adhesive had to be made, as for some measurement series the conditions are very humid. Therefore, not all types of glue can be used in such an environment, as they could dissolve and make the sample slip under tension. In addition, the adhesives must not be absorbed into the hair, as this could potentially influence the measurements. A variety of adhesives ranging from different types of super glue to epoxy and regular glue was tested. Resulting in the UHU gel as the glue of choice. The testing process in detail is explained in section 4.2.

3.3. SAXS

SAXS experiments were performed using a Bruker AXS Nanostar equipped with a 2D detector (Våntec 2000) and two image plates (Fuji FLA 7000). As the scattering angles are large, the successful detection can only be achieved by using image plates, which are placed at a distance of 51.7 mm behind the sample. During the planning phase different setups have been tested, with the Våntec 2000, which is used in most of the other measurements with this apparatus. But all of them were unsuccessful, as either the observed angles were too small or the setup was just too complicated. The disadvantages of the image plates, however, are that one has a less precise repeatability of the scattering intensities and that one cannot use a script to automatize the measuring process. The plates have to be removed from the sample chamber after each single measurement and put into a special scanner from FujiFilm to read out the data. This scanning takes quite some time and after that the image plates have to be cleared using a special image plate eraser, which takes again around 5 min. To speed up the measuring time, two image plates have been used but this creates the problem, that they have slightly different light sensitivity and the center is also shifted. However these inconveniences were accepted, as this setup provides the needed angular range and it is also still possible to locate and position the sample correctly with the detector and the positioning table.

3.4. Experimental Setup

The final setup consists of the X-ray source which produces Cu K-α X-rays with a wavelength of $\lambda = 1.5418$Å. Part of the beamline (source to chamber) is under vacuum, for experimental reasons the sample chamber is at normal pressure. Therefore the entrance hole of the X-rays and exit to the detector are sealed off using a metal ring with a Kapton window. Inside the sample chamber there is a movable platform where the humidity chamber is mounted on top. There is also the slot for the image plate. As the image plates also react to the light in the room, the window of the sample chamber is covered with a metal plate. The gas detector is also in use for positioning the sample in the correct spot, so that the X-ray beam hits the hair sample. For the positioning the Scan function in the SAXS software is used. A short test image can be taken with the detector to double check if the sample is hit by the X-ray beam or not. The picture of the detector gives the diffraction rings of the hair and as they have a characteristic orientation, it can easily be verified as the sample.

To gain thermodynamically stable conditions inside the humidity chamber, the chamber

has to be heated prior any experiments for at least 30 min. The temperature of the water reservoir is set to 25 °C. With the program *mhg* and *mhgctl* the data of the MHG is logged and the humidity level set. After the thermodynamic equilibrium is met and the humidity is stable, the measuring process can start.

For this theses measurement series for four different values for the relative humidity were performed. These are at 20%, 40%, 60% and 80% relative humidity. One measuring cycle starts with the sample at 0% strain. After the acquisition, the strain gets increased using the Doli software to 10% strain and the sample is measured again. This process is repeated for 20% strain and then the strain level is increased by 5% steps between each measurement up until 60%. For calibration purposes an Al_2O_3 sample was measured afterwards with the rear panel of the humidity chamber open, such that more diffraction rings of the sample are visible on the image. Another necessary measurement that needs to be taken is the background of the chamber. This is recorded with the closed humidity chamber at the set humidity level. Each of the measurements has an exposure time of 30 min, except the calibration sample, which is measured in 10 min.

4. Results

This chapter explains the steps in the analysis of all the collected data. In the first part the evaluation of the compliance of the tensile machine and its influence on the further measurements is discussed. Additionally the behavior of the different types of glue is shown. The second part of the chapter contains the measured spectra of the hair samples.

4.1. Compliance of the Tensile Machine

When a tensile test machine is used, then not 100% of the deformation is on the specimen, as the machine itself also undergoes some deformation. During the measurement the motor of the machine moves the top crosshead and displaces the specimen. The displacement distance l is measured by the program with an encoder in the machine. However this distance gives the total system deformation and therefore needs to be corrected to get the distance between the endpoints of the sample. This distance can be calculated using the formula:

$$l_{corrected} = l_{measured} - C \cdot F \tag{4.1}$$

where $d_{measured}$ is the measured distance from the program, C is the machine compliance, and F is the measured load force. To obtain C a series of measurements needs to be done. The idea here is to measure a very stiff thick wire and from the measured forces and displacements the compliance is calculated. It is important, that the material is stiff, as otherwise the effect of the compliance is too low. For this thesis a molybdenum wire with a diameter of $d = 600\,\mu m$ is used. The wire has a clamping length of $L = 17\,mm$. For this test the program is set to slowly expand the sample for a total displacement of $l = 0.2\,mm$ with a speed of $0.01\,mm\,s^{-1}$. After finishing one run, the setup is reset by unscrewing the lower clamp, moving the crossheads back to the original position and fixating the wire again. The whole process is repeated four times to get a set of five data files. With a small Python program the data is analyzed, by fitting a linear function in the elastic expansion part of the displacement-load plot. In figure 4.1 the plot of one of the tests is shown. Here the x-axis shows the displacement in mm and the first linear growing part of the data points is the elastic part of the deformation. At a displacement

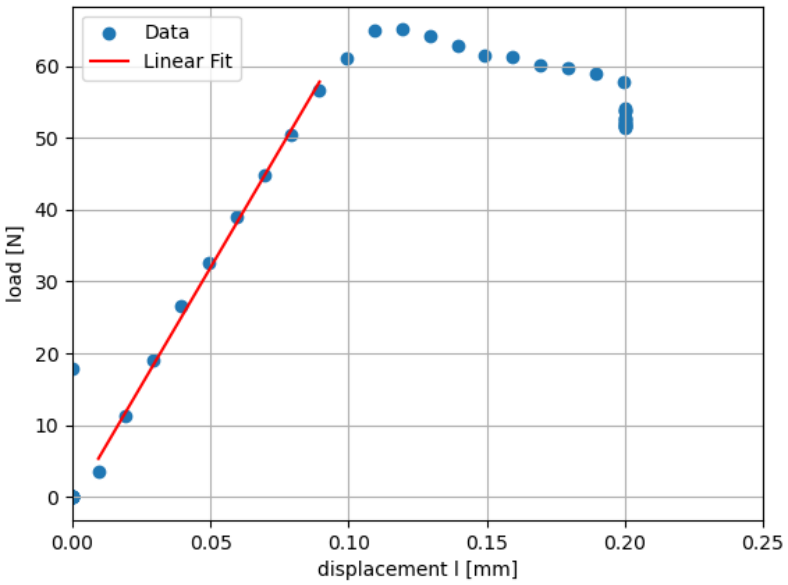

Figure 4.1.: Displacement-load plot of one of the tensile tests with the molybdenum wire.

of about 0.11 mm the behavior of the curve changes. This is a combination of plastic deformation and that the wire is slipping out of the clamps. For the determination of the compliance, the following formula is used:

$$C = \frac{1}{k_{apparent}} - \frac{L}{k_{wire}} \tag{4.2}$$

where k is the stiffness of the material. The apparent stiffness is obtained as the slope of the linear fit. Here the five slopes are averaged and as the uncertainty the standard error is used. This gives a $k_{aspparent} = (680 \pm 12)\ \mathrm{N\,mm^{-1}}$. To calculate the stiffness of the wire k_{wire} the Young's modulus of molybdenum is needed, which is $E_{\mathrm{Mo}} = 320$ GPa, as well as the cross-sectional-area and the clamping length L.With these values the stiffness is:

$$k_{wire} = \frac{EA}{L} = 93\ \mathrm{N\,mm^{-1}} \tag{4.3}$$

This results in a compliance of $C_{machine} = (1.47 \pm 0.03)10^{-3}\ \mathrm{mm\,N^{-1}}$.

4.2. Testing of different glues

The idea on how to test the different glues is similar to the determination of the compliance in the previous section. However, this time the wire is glued on a paper frame, like the actual hair samples. This test is also focused on the behavior of the glues, rather than measuring precise numbers. Therefore, for each glue the measurement is performed once at very low (around 10-15% RH) and then at a very high (100% RH) relative humidity. The reason behind, that this should give an overview if a certain glue decomposes under moist conditions or not, as this would lead to the sample slipping out of the paper frame. If this happens, then the load and displacement measurements during the experiment, would be completely off. The clamping length in this experiment is $L = 10$ mm, as the same sized paper frames are used as for the hair samples. The main was focus is to determine, whether the UHU gel super glue or the one from Loctite performs better under the given conditions. Additionally a regular paper UHU glue and epoxy glue also by UHU are tested, just to see some differences. As visible in the figure 4.2 the Loctite super glue is the strongest. The gel and epoxy glue perform relatively the same and as expected the regular paper glue can't withstand the wet condition. Interestingly the tensile test plot also shows a steeper slope for the Loctite compared to the other glues. This can be explained as the regular Loctite is made of cyanoacrylate, whereas the epoxy and regular paper UHU are made of a different material, which is not as stiff as cyanoacrylate. The UHU Gel is also made of cyanoacrylate, but as it is a gel glue it has some additional chemicals to make it more flexible. This results in a less steep curve in the tensile test plot. However the glue of choice is the gel, as it is thicker than the very liquid Loctite. This is a potential problem, as the glue possibly can be soaked into the hairs, which then interferes in the diffraction patterns. The epoxy is not interesting to use, as this type of adhesive needs a long time for curing. As this is impracticable for preparation of straight and therefore slightly stretched bundles of hair, this glue was not selected for the experiments.

4.3. WAXS Measurements of Hair

The hair samples were recorded in several individual measurement series. The humidity chamber was first adjusted and calibration measurements were carried out. Then the measurements began at a fixed humidity and increasing strain.

The measured files are 2D images, where the pixels store the intensity at that position. To get a 1D spectrum, the 2D image needs to get integrated. Since the hair exhibits

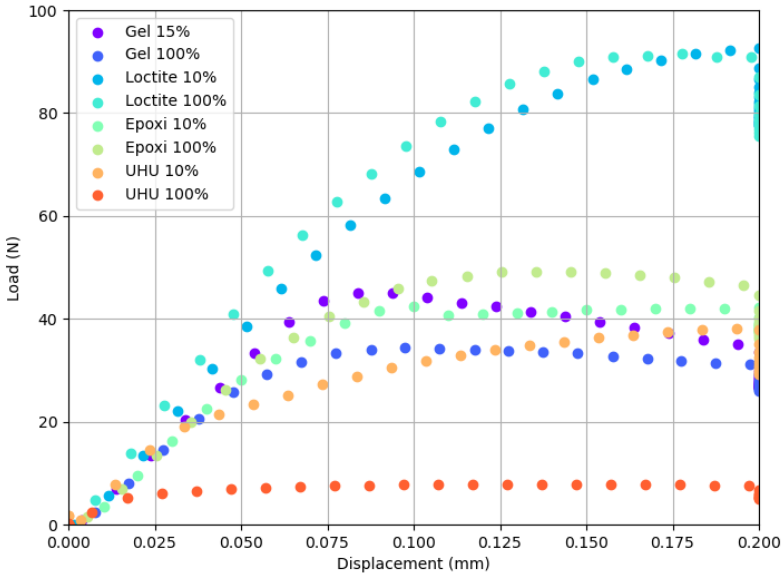

Figure 4.2.: Displacement-load plot of the tensile tests of the molybdenum wire using different glues and varying humidity conditions.

anisotropic scattering, the radial profile cannot be integrated over the entire 360° azimuthal angle. Therefore, smaller sections are chosen. For the horizontal peaks (perpendicular to the orientation of the hair) the section starts at an azimuthal angle of 75° and ends at 105°.[1] As the peaks show symmetrical symmetry around the hair, another integral can be calculated starting at an azimuthal angle of 255° and ending at 285°. For the integration all azimuthal angles are stored in one bin and for the radial resolution one bin per pixel was chosen. For all the integrations the program FIT2D [22] was used. The peaks parallel to the hair orientation were integrated separately and although they also show symmetrical behavior, only one section was used for analysis. This is because the other side is blocked off by some parts of the humidity chamber. The azimuthal angles for the integration start at 155° and end at 205°.

4.3.1. Challenges of the measurements

When measuring with image plates, one has to be very careful, as there are many pitfalls in the experiments. One problem is that the frames of the image plates sometimes got

[1] Because the image plate reader rotates the files by 90°, the peaks appear on the vertical axis in the images.

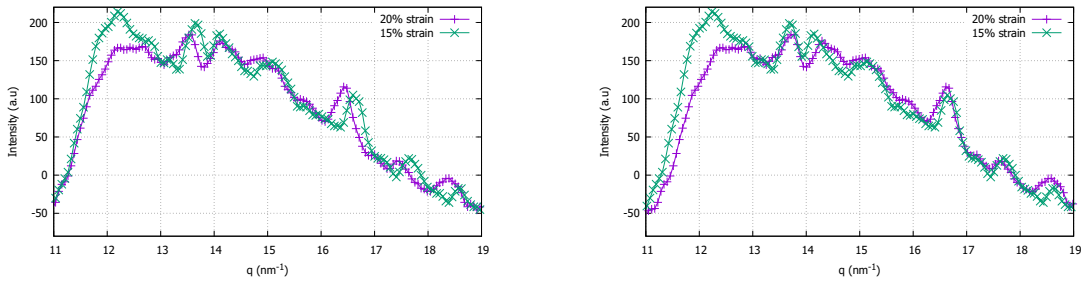

(a) Before correction: The spectra are shifted with respect to each other.

(b) After correction: The spectra are correctly aligned and no longer shifted with respect to each other.

Figure 4.3.: Two spectra of the measurement series at 60% relative humidity. Subfigure (a) shows that the two peaks at around $q = 13.7$ nm^{-1} and $q = 16.5$ nm^{-1} clearly show that one spectrum is shifted with respect to the other. Subfigure (b) displays the corrected alignment. The spectra are background corrected using the polynomial function in formula 4.5.

stuck a little when they were inserted into the rail. This can cause them to be displaced by a few millimeters and as result the scanned images by the reader always have a slightly different beam center. To correct this, one would need to define the beam center for each measurement individually, as integrating all of them with the same parameters, would lead to the spectra being slightly shifted to another. In figure 4.3a two spectra of the measurement series at a relative humidity of 60% are plotted. The spectra are acquired at different strains and with different image plates and integrated using the same parameters for the beam center and radius of the cake segment. The figure shows that this leads to spectra, which are slightly shifted with respect to each other. To ensure accurate peak alignment and facilitate a proper comparison, a correction for this displacement must be applied. In order to align all measured files, the entire spectrum is shifted on the q-axis using a Python program (see listing A.1 in the appendix). There are two clearly visible peaks from the Kapton in the spectrum, which are used for the shifting process. These peaks are useful for this case, as they are not influenced by the different strains and also prominent in the spectrum. But since the Kapton window is located at the entrance of the beam line into the sample chamber, the detector distance is different, as the humidity chamber with the sample is in the middle of the sample chamber. Because of that the peak is not measured at the literature value for the Kapton peaks but at a smaller q. For this measurements the value is assumed at $q = 13.7$ nm^{-1} and all the spectra are shifted, such that the Kapton peak is at that position. The program reads the individual spectra

and fits a split Gaussian function in a selected range. The function has the form of:

$$f(x;\mu,\sigma_1,\sigma_2) = \begin{cases} \frac{\sqrt{\frac{2}{\pi}}\exp\left(-\frac{(x-\mu)^2}{2\sigma^2}\right)}{\sigma+\sigma_2}, & x < \mu \\ \frac{\sqrt{\frac{2}{\pi}}\exp\left(-\frac{(x-\mu)^2}{2\sigma_2^2}\right)}{\sigma+\sigma_2}, & x \geq \mu \end{cases} \tag{4.4}$$

It then calculates the offset in q-direction Δq between the peak center of the fit and 13.7 and shifts the whole spectrum by that value. The result is that all spectra are then correctly aligned, as shown in figure 4.3b.

Although it is possible to align the spectra with the program and counteract the effect of the displaced image plates, one still has to be careful and push the plates completely in the frame, which normally can be heard by a clicking sound. Otherwise it can happen, that the displacement of the image plates is so large, that the beam is hitting the image plate directly. Normally there is a large enough hole in the middle of the plates, where the beam either goes through and can then be detected at a second detector or it just hits the panel, where the image plate is stuck on. However if it hits the image plate the image plate reader has some problems reading the over saturated pixel and creates very bright lines, which negatively impact the whole measurement. This unfortunately happened in the measurement series at 80% relative humidity for three images. These can therefore not be used for the evaluation. In figure 4.4 one can see the bright lines that overpower the regular diffraction reflexes in intensity.

Another characteristic of image plates, which can cause issues, is that they have a certain intensity threshold. This means that there is a required minimum intensity for the pixel. The accumulation of intensity is also not linear for image plates after a certain time of irradiation. Therefore, one has to decide, if a longer measuring time is necessary because of weak signals and if the effect of a non-linear signal acquisition does not make the uncertainty to large.

But not only the image plates themselves can cause issues. The image plate reader is also a possible error source. One minor thing to keep in mind is, that it rotates the images by 90° clockwise. This is by itself not a big deal but one just has to be careful about it. The read out however can fail sometimes, resulting in bright and dark sprinkles all over the image. This can be easily resolved by just doing another scan of the plate. Figure 4.5 shows how the images look different, when affected by a failed read out. As visible in the right picture, There are multiple bright spots, which should normally not appear as shown in the rescan in the left image. The other difference between both of the

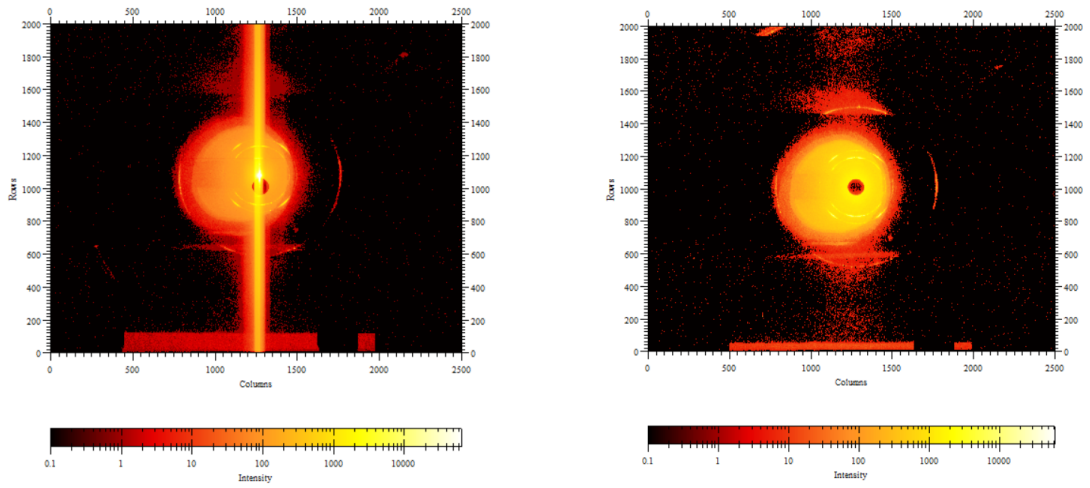

Figure 4.4.: Both images are taken from the measurement series of 80% relative humidity. The left one is at a strain of 55% and the right one at 35%. The right one is showing the normal diffraction pattern of the experiment as expected and the left one has a large bright bar across the picture caused by the image plate being incorrectly positioned.

pictures is that the intensity of the brightest pixels in the right one is about 10 times lower. One more issue that can occur using the image plate reader is, that the choice of the read out grid matters. In the measurement series at 80% relative humidity the scanning process stopped or failed multiple times, which was possible to fix by restarting the reader. However there is a better solution by adjusting the grid size in the program of the reader a little bit. With this change the other measuring series did not encounter this problem. The most likely reason for this is, that there is a dead pixel in the reader, which can cause issues and by setting the grid, such that it will not use that specific pixel, the scanning process works normally. However, one has to keep in mind, that by changing the grid size of the reader, the image size also changes. As a result the beam center is at different coordinates.

There was another issue that occurred during the measurements, which made it necessary to redo one whole measurement series. While setting up the humidity generator for the series at 40% relative humidity, the container with distilled water was not properly installed, preventing any water from passing through the valves. This caused several problems. First, because there was no water passing through the pipes, the MHG generator was only pumping nitrogen gas into the humidity chamber, which resulted in lowering the humidity under the desired level. Due to the long measuring times, this was not

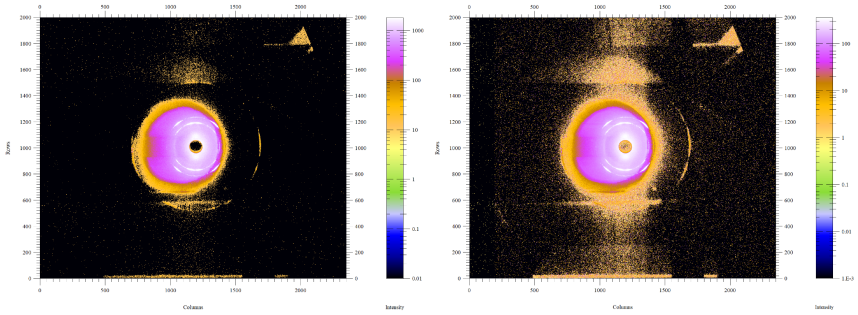

Figure 4.5.: Two images of the measurement series at 20% relative humidity. Both were measured at a strain of 0%. The left image is after rescanning a second time with the image plate reader. The right one shows how the image is affected, if the reader has some issues scanning the plates correctly.

recognized immediately. As a result, the humidity generator tried to pump more water into the mixer to restore the desired humidity level. However, as the pump was unable to draw in water through the valves, a vacuum was created, which led to the second problem. When the water reservoir was reinserted correctly, the pump sucked in far too much water, which resulted in the mixer being flooded. The sponge inside was then completely saturated, causing water to splash into the humidity chamber and the hair sample to become wet. To solve these problems, the excess water had to be removed from the tubes, the sponge dried and a new sample inserted. As it was not possible to determine exactly when the results were affected by this error, hence the entire series of measurements was repeated.

4.3.2. Background correction

As the next step the background needs to be subtracted, which is handled by another Python program. It fits the background by using the following function:

$$f(q) = c + aq^{-n} \tag{4.5}$$

This approach of fitting a polynomial function does work for a certain range in q. The problem here is that the background for these measurements has a second feature, a broad peak probably arising from clusters of amorphous molecules within the sample. This background is not subtracted by the polynomial function (eq. 4.5). When only fitting and subtracting formula 4.5 in the interval from $q = 6.2$ nm^{-1} to $q = 24.0$ nm^{-1}, the resulting spectra is illustrated in figure 4.7b. The figure shows, that there is still a

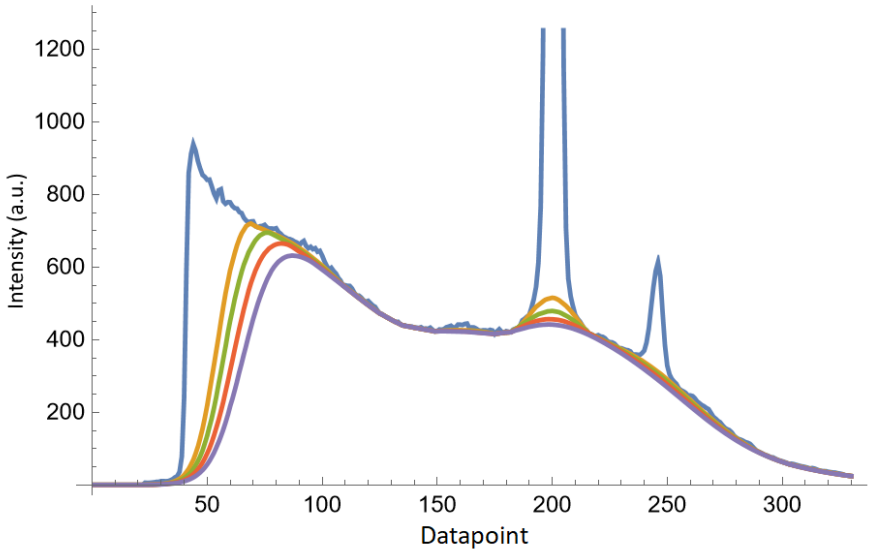

Figure 4.6.: Spectrum of the measurement at 80% relative humidity and 0% strain in vertical orientation. The plot shows the original spectrum and four different background functions obtained with `EstimatedBackground` in Mathematica.

large broad background structure. In order to obtain a better background correction, one could perform another fit with the polynomial function. However, in order to precisely determine the maximum in q (and not the absolute intensity), a different approach was chosen, as another polynomial fit probably would interfere with the peak at $d = 0.515$ nm ($q = 12.1$ nm^{-1}). Therefore, the background was calculated using the built in `EstimatedBackground` function in Mathematica. This function calculates the background of the provided spectral data and has a parameter, which controls how many features in the spectrum should be preserved. In figure 4.6 one can see how different values for the parameter, which handles the peak conservation, changes the background estimation. For the plot values of 7, 8, 9 and 10 are chosen, where 10 is the purple line and 7 the orange one. For the horizontally measured spectra a value of 8 was chosen. For the spectra in the vertical orientation a value of either 8 or 9 was chosen. Figure 4.7c displays the background corrected spectrum using this approach and compares it to the uncorrected as well as the corrected spectrum using a polynomial function. [23]

4.3.3. Calibration

For the calibration a sample of aluminum oxide powder Al_2O_3 is put into the humidity chamber. In order to get more diffraction rings in the image, the rear side of the chamber

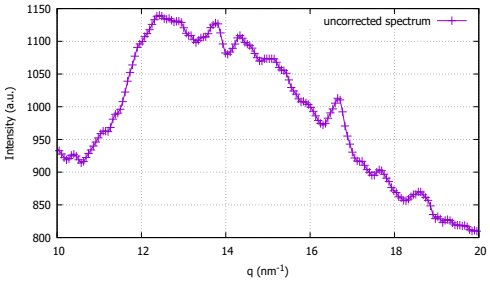

(a) Uncorrected original spectrum.

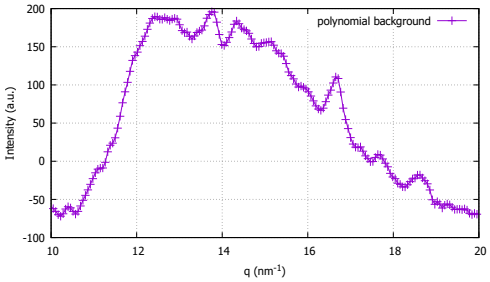

(b) Background corrected spectrum using a polynomial approach.

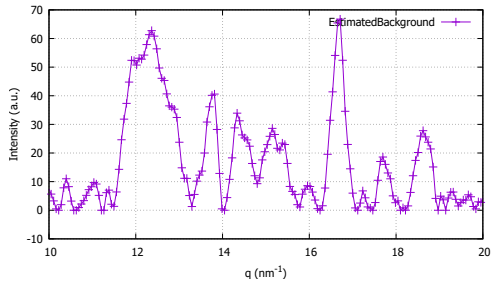

(c) Background corrected spectrum using `EstimatedBackground` from Mathematica.

Figure 4.7.: Comparison of three spectra of the measurement at 60% relative humidity and 20% strain. In subfigure (a) the background uncorrected spectrum is shown, in (b) the background correction was performed using a polynomial function (eq. 4.5) and in (c) the background was corrected using the Mathematica function `EstimatedBackground`.

is left open. For this measurement the exposure time was only 10 min instead of the 30 min for the hair samples. This is because alumina has a characteristic, well-defined and strong scattering signal due to the high structure factor. In contrast, biological samples, such as hair, generally have weaker and more complex scattering patterns due to lower atomic scattering factors and a more or less ordered or even disordered arrangement of different molecules instead of a regular arrangement of atoms. Because of this difference, it is sufficient to measure the calibration sample only a third of the time, while still obtaining high quality data. With the program FIT2D the calculation of the detector distance was performed. The resulting distance is then $d_{IP} = 51.7$ mm.

4.3.4. 80% relative Humidity

The first measurement series was conducted at a relative humidity of 80%. Before the first image can be taken, the MHG needs to be connected and the correct humidity level has to be set. After that one has to wait about 20 min to ensure that the humidity chamber is in thermal equilibrium. The first measurement is acquired at a strain of 0% on the hair and the second one with 10%. After that, the strain is increased in 5% steps between measurements. All of the acquired data is then treated, as mentioned before, by integrating with FIT2D to generate 1D spectra for the horizontal and vertical oriented peaks. After that shifting in q to align the spectra, as well as subtracting the background is done. The final spectra are then plotted and the relevant peaks analyzed. Comparing with previous studies such as by Kreplak et al. in vertical orientation a peak at $d = 0.515$ nm ($q = 12.1$ nm^{-1}) should vanish with increasing strain and a new one at $d = 0.33$ nm ($q = 18.9$ nm^{-1}) emerge. For the horizontal orientation the literature predicts a peak, which appears at $d = 0.465$ nm ($q = 13.5$ nm^{-1}) when increasing the strain. [3, p. 640]

Vertical orientation

In the vertical orientation parallel to the hair one can see that the peak of $d = 0.515$ nm ($q = 12.1$ nm^{-1}) is vanishing at higher strains (shown in figure 4.8). The second interesting peak in this orientation at $d = 0.33$ nm ($q = 18.9$ nm^{-1}) appears at higher strains, but it cannot be verified for sure, as the peak is very low in intensity. The vertical dashed lines should show the expected location of the peaks, but as the whole spectrum is shifted, the position of the peaks can be slightly different. In the figure one can also clearly see, that the spectra at 45%, 50% and 55% are looking very different and have no valid data. This is because, as mentioned before, there was an issue operating the image plates.

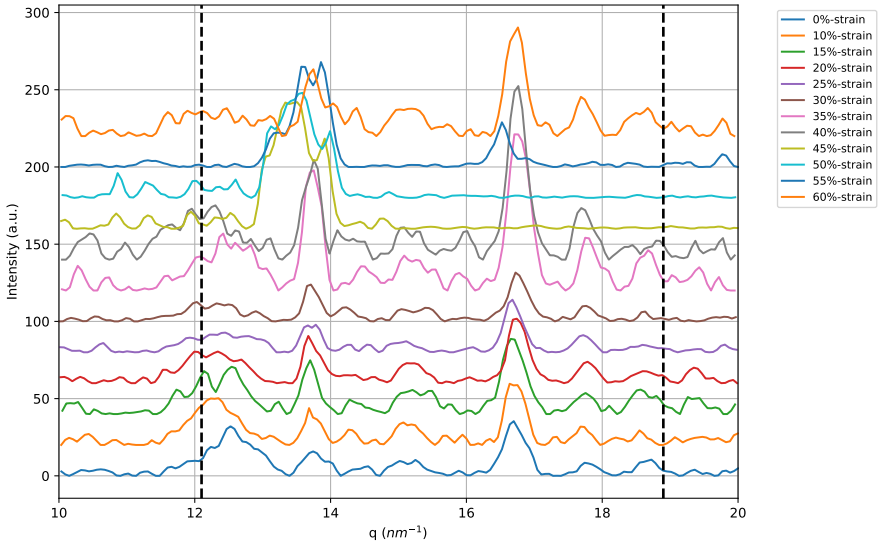

Figure 4.8.: Waterfall plot of the measurement series at 80% relative humidity in vertical orientation. The two vertical lines show the location of the expected peaks at $q = 12.1$ nm^{-1} and $q = 18.9$ nm^{-1}.

Horizontal orientation

Figure 4.9 shows the evaluated data of the spectra. In the horizontal orientation there is only the peak of $d = 0.465$ nm ($q = 13.5$ nm^{-1}). Unfortunately this peak cannot be seen as the peak of the Kapton is located at $q = 13.7$ nm^{-1} and thus covers the peak of interest, as the Kapton peak has a very high intensity. Besides the very intense Kapton peak, there no other peak can be identified. In the figure one can see again, that two spectra are unusable, due to the error when inserting the image plates.

4.3.5. 60% relative Humidity

Vertical orientation

Figure 4.10 shows the evaluated data of the spectra in this orientation. In this series the peak at $d = 0.515$ nm ($q = 12.1$ nm^{-1}) flattens again. The second peak cannot be identified unambiguously. There is an intensity maximum in the vicinity of $q = 18.9$ nm^{-1}, but at a slightly different position. Additionally, it does not evolve, but is rather constant.

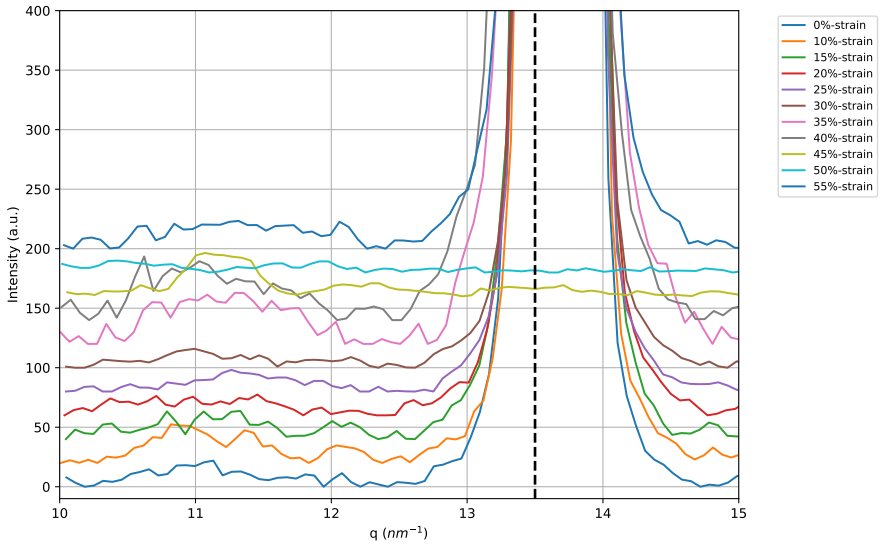

Figure 4.9.: Waterfall plot of the measurement series at 80% relative humidity in horizontal orientation. The vertical line shows the location of the expected peak at $q = 13.5$ nm^{-1}.

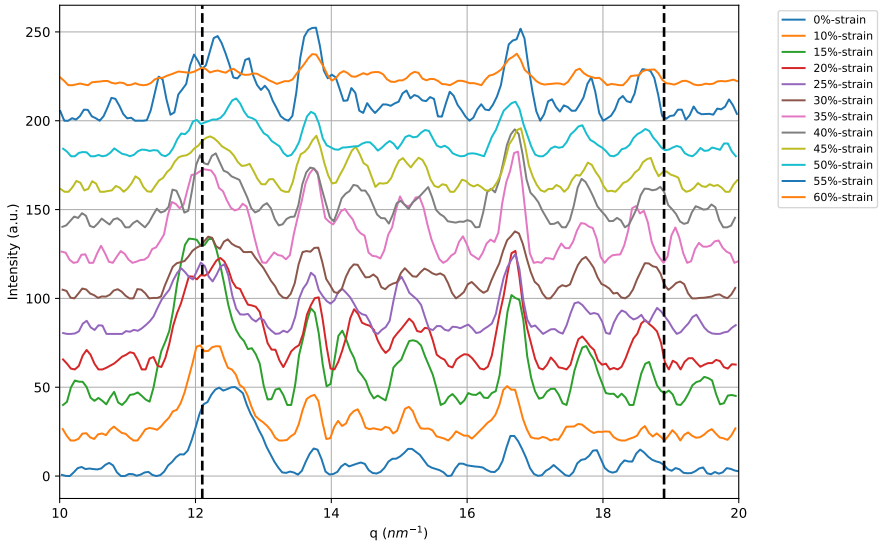

Figure 4.10.: Waterfall plot of the measurement series at 60% relative humidity in vertical orientation. The two vertical lines show the location of the expected peaks at $q = 12.1$ nm^{-1} and $q = 18.9$ nm^{-1}.

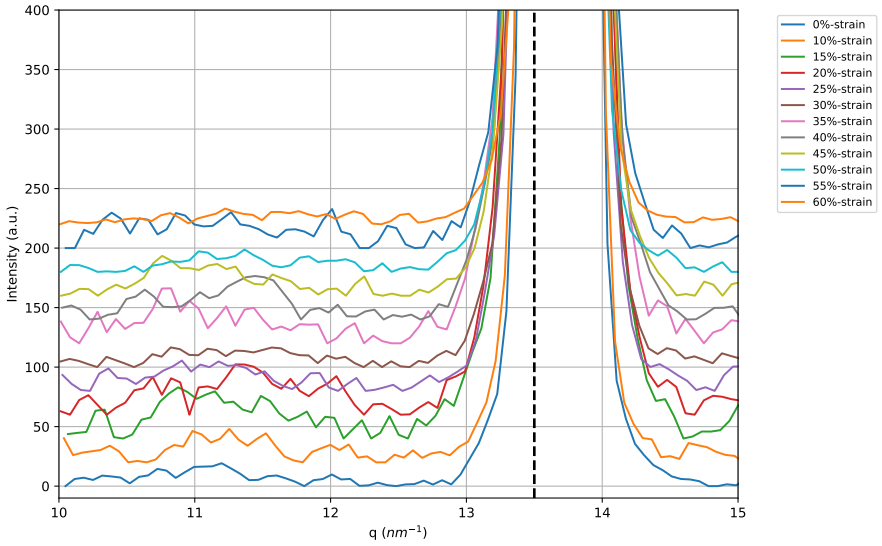

Figure 4.11.: Waterfall plot of the measurement series at 60% relative humidity in horizontal orientation. The vertical line shows the location of the expected peak at $q = 13.5$ nm^{-1}.

Horizontal orientation

Figure 4.11 shows the evaluated data of the spectra in this orientation. Just like for the measurement at 80% relative humidity, the Kapton peak is too prominent and at a position, where it masks the expected peak at $q = 13.5$ nm^{-1} ($d = 0.465$ nm). Thus, the expected peak from the α-to-β transition cannot be separated from the Kapton background.

4.3.6. 40% relative Humidity

Vertical orientation

Just like in the 80% and 60% relative humidity measurements the first peak at $q = 12.1$ nm^{-1} flattens with increasing strain and the second peak at $q = 18.9$ nm^{-1} cannot be verified. There is a peak near the expected $q = 18.9$ nm^{-1} but instead of rising with higher strain, it is rather vanishing. Figure 4.12 shows the evaluated data of the spectra in this orientation.

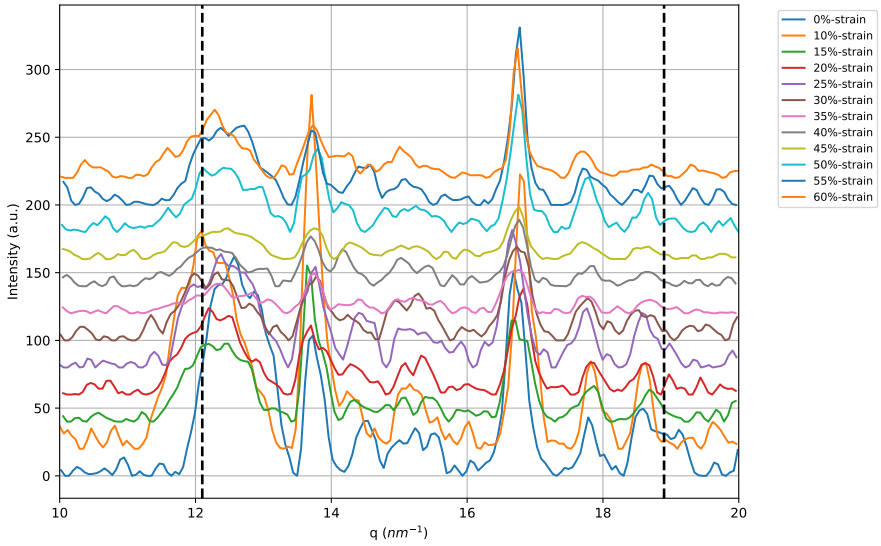

Figure 4.12.: Waterfall plot of the measurement series at 40% relative humidity in vertical orientation. The two vertical lines show the location of the expected peaks at $q = 12.1$ nm^{-1} and $q = 18.9$ nm^{-1}.

Horizontal orientation

As in the other measurement series, the Kapton window peak masks the position of the peak to be observed at $q = 13.5$ nm^{-1} in this humidity setting as well. Figure 4.13 shows the evaluated data of the spectra in this orientation.

4.3.7. 20% relative Humidity

Vertical orientation

For this measurement series, one can no longer see that the peak at $q = 12.1$ nm^{-1} vanishes as observed in the measurements at higher relative humidity. The peak from the α-keratin protein structure is strong and present even at the highest strain of 60%. Figure 4.14 shows the evaluated data of the spectra in this orientation.

Horizontal orientation

Also in this series of measurements, masks the Kapton window peak the position of the expected peak at $q = 13.5$ nm^{-1} and it therefore cannot be observed. Figure 4.15 shows the evaluated data of the spectra in this orientation.

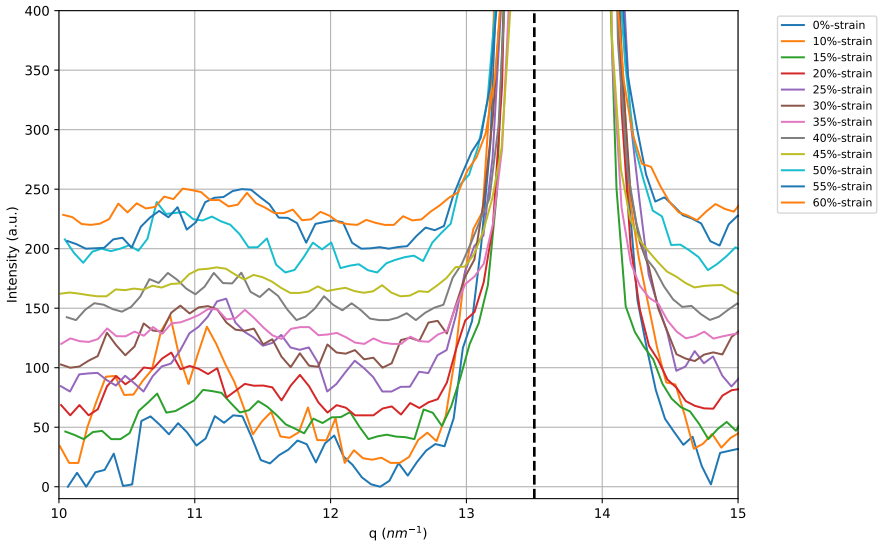

Figure 4.13.: Waterfall plot of the measurement series at 40% relative humidity in horizontal orientation. The vertical line shows the location of the expected peak at $q = 13.5$ nm^{-1}.

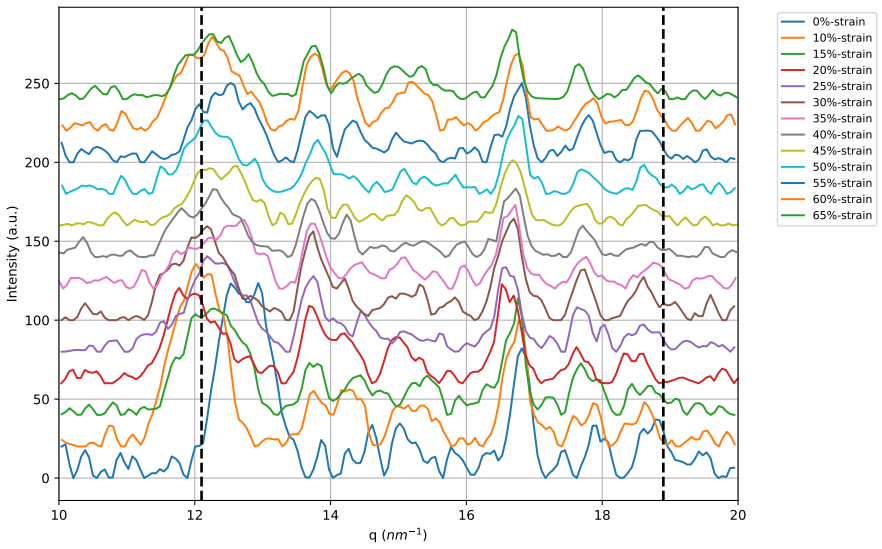

Figure 4.14.: Waterfall plot of the measurement series at 20% relative humidity in vertical orientation. The two vertical lines show the location of the expected peaks at $q = 12.1$ nm^{-1} and $q = 18.9$ nm^{-1}.

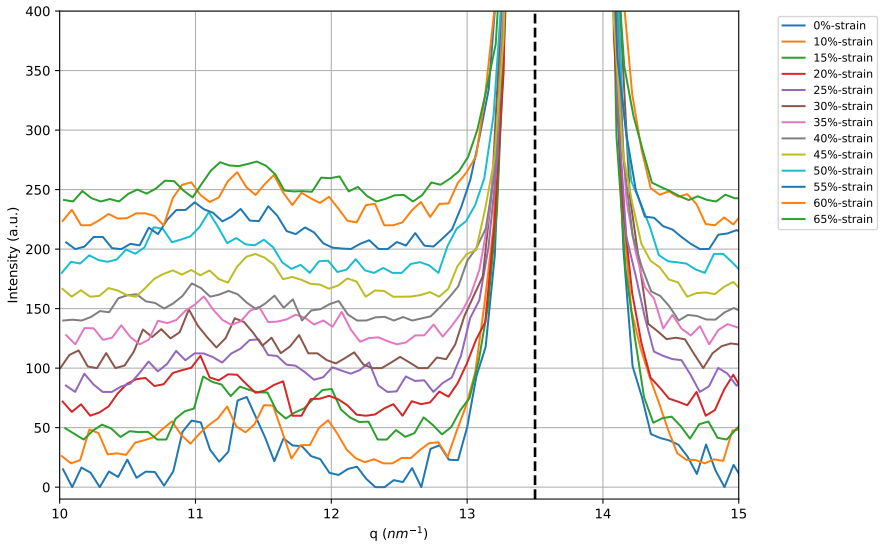

Figure 4.15.: Waterfall plot of the measurement series at 20% relative humidity in horizontal orientation. The vertical line shows the location of the expected peak at $q = 13.5$ nm^{-1}.

5. Discussion

The aim of this thesis was to show, whether it is possible to measure the effect of the α-to-β transition on the X-ray pattern in a laboratory setting and how it behaves when measuring human hair. Before the measurements could take place, it was necessary to think about and test various setups. Most of them were not possible to realize because the detector distance was too long and there was no option to reduce it further. An idea was to measure with a different detector (EIGER2 R 500K by Dectris), but this was also not feasible, because that detector would have only been able to measure one orientation at a time due to its rectangular shape. But as the measurement required evaluation of the horizontal as well as the vertical axis, another setup was needed. All of this lead to the choice of the image plates for the detection of the signals. However, this lead to various other challenges. Some of them were easy to handle, like changing the rotating base part of the humidity chamber for easier access to the samples. Other problems occurred during the measurements, with some of them being recoverable, like the rescanning of the image plates in case of the read out error. The major problem however is, the Kapton window. It has some useful characteristics, as it can be used as a prominent peak to align the spectra in q and the main purpose is to separate the beam line from the sample chamber, such that the beam line stays in vacuum. The disadvantage is that the intense Kapton peak is covering the peak at $d = 0.465$ nm ($q = 13.5$ nm^{-1}) in horizontal orientation. Therefore it cannot be verified, if that peak is measurable with this setup, if it does show at all under the experimental conditions or if it is not present. A solution to this problem can be achieved in two different ways. The first one is not really realizable in our SAXS equipment, as it needs changing the distance between image plates and Kapton window. However, the image plates are fixated by rails in the sample chamber and the Kapton window is also at a fixed position. The other opportunity is, changing the Kapton to a different type of polymer. Due to the change of material, the peaks of this window would also be at a different position in the diffraction pattern, or even disappears, if an amorphous polymer is used.

Vertically, parallel to the hair sample orientation, the measured data appears more promising. This is because different peak positions, which are not covered by the Kapton,

are being considered. Of the two peaks to be investigated, the expected behavior under changing conditions could only be observed for those at $d = 0.515$ nm ($q = 12.1$ nm^{-1}). In the measurement series of 80%, 60% and 40% relative humidity the decline of that peak (or the absence in the case of 80% relative humidity), when increasing the strain from 0% up to 60%, can be noticed. For the other peak at $d = 0.33$ nm ($q = 18.9$ nm^{-1}) this cannot be verified. In the 80% relative humidity series, it can possibly be seen, but as there was an issue with the measurement, there are some important spectra not showing relevant data. With the assumption that the measurements at 40% and 60% strain are showing the expected behavior of a rising peak, it is crucial to remeasure at this humidity level, to ensure proper data. At lower humidity levels the rise of the peak cannot be observed. This leads to the assumption that either a higher humidity or temperature is needed. Or if the only chance of detection is when using steam and therefore extreme conditions of $T > 100\,^{\circ}$C and 100% relative humidity. In order to test, if a different setting with steam at higher temperatures is the key for the detection of the 0.33 nm peak, it is required to build another humidity chamber, as the one used in this thesis is not capable of generating steam.

Relying on the image plates with this setup has some major disadvantages. The measuring process becomes a lot more work intensive, as it cannot be automated and various issues can occur as mentioned. Despite all these drawbacks, the results were still reasonable and partially met the expectations. However, due to problems like the threshold, shifted spectra, failed measurements and the necessity of manually measuring, it is strongly advised to build a working setup with a detector instead. As this would most likely produce better datasets with the possibility of smaller steps in strain, as the process can be monitored remotely.

Another interesting point is that Cao et al. [24] suggested that the α-to-β transition is not happening immediately after the deformation. Due to the long measuring time because of the low intensity signal in combination with the use of image plates, the sample in this thesis was also measured over some time after stretching, similar to the work of Cao et al. However, they have again used steam for the setting time. For another measurement it could be interesting to measure at different times after stretching e.g. 30 min, 60 min and 120 min later. One more idea is how the hair behaves if relaxed after a certain time at a specific extension.

Abstract

In this master's thesis, human hair is examined in situ under tensile stress and humidity using wide-angle X-ray scattering (WAXS). The aim is to provide evidence for the occurrence of the α-to-β transition in the keratin of hair. Since hair has significant societal relevance, knowledge about its structural properties and behavior is of great interest. As this transition has so far only been detected in synchrotron facilities, the question arises whether it is also possible to measure it in a laboratory setting.

For this purpose, the Bruker Nanostar SAXS system was used, and a suitable experimental setup was implemented. To detect the scattering patterns, image plates had to be used for various reasons. These plates are positioned at a distance of 51.7 mm from the sample. The hair samples are clamped into a tensile testing machine within a humidity chamber. During the measurements, both humidity and tensile stress applied to the hair are varied to determine the conditions for the occurrence of the α-to-β transition.

Compared to previous studies [1], this project not only refrained from using a synchrotron but also used human hair. Instead of steam, the hair was humidified using a humidity generator. Due to the lower extensibility of human hair compared to horsehair, only tensile strains of up to 60% could be achieved. The measured intensities were analyzed in both horizontal and vertical orientations. The results show that the expected behavior could be partially observed. However, not all diffraction reflexes are detectable in the recordings, as some are not visible due to the setup. For another peak that cannot be clearly observed, a possible explanation is that steam, and thus a higher temperature, is an important factor for the occurrence of the α-to-β transition.

Kurzfassung

In dieser Masterarbeit werden menschliche Haare in situ unter Zugbelastung und Feuchtigkeit durch Röntgenweitwinkelstreuung (WAXS) untersucht. Dabei soll ein Nachweis über das Auftreten des α- zu β-Übergangs im Keratin der Haare erbracht werden. Da Haare eine wichtige gesellschaftlichen Relevanz haben, sind das Wissen über ihre strukturelle Beschaffenheit und ihr Verhalten von großem Interesse. Da dieser Übergang bisher nur in Synchrotronanlagen nachgewiesen wurde, stellt sich die Frage, ob es auch die Möglichkeit gibt, ihn im Labor zu messen.

Dafür wurde die Bruker-Nanostar-SAXS-Anlage verwendet und ein passender Versuchsaufbau realisiert. Zur Detektion der Streumuster mussten aus diversen Gründen Imageplates verwendet werden, die sich in einem Abstand von 51.7 mm zur Probe befinden. Die Haarproben werden in eine Zugmaschine innerhalb einer Feuchtekammer eingespannt. Dabei werden im Verlauf der Messungen sowohl die Feuchtigkeit als auch die Zugbelastung am Haar variiert, um die Bedingungen für das Auftreten des α- zu β-Übergangs bestimmen zu können.

Die Messungen dieses Projekts haben im Gegensatz zu vorherigen Studien [1] nicht nur auf das Synchrotron verzichtet, sondern auch menschliche Haare verwendet. Anstatt von Dampf wurden die Haare mittels Feuchtegenerator befeuchtet. Aufgrund der geringeren Dehnbarkeit von menschlichem Haar im Vergleich zu Pferdehaar konnten nur Belastungen von bis zu 60% Dehnung erzielt werden. Die gemessenen Intensitäten wurden sowohl in horizontaler als auch vertikaler Orientierung ausgewertet. Die Resultate zeigen, dass das erwartete Verhalten teilweise beobachtet werden konnte. Jedoch sind nicht alle Beugungsreflexe in den Aufnahmen nachweisbar, da sie einerseits aufgrund des Aufbaus nicht sichtbar sind. Für einen weiteren Peak, der nicht eindeutig beobachtet werden kann, könnte eine mögliche Erklärung sein, dass Dampf und damit auch eine höhere Temperatur ein wichtiger Faktor für das Auftreten des α- zu β-Übergangs ist.

Bibliography

[1] L. Kreplak, J. Doucet, and Fatma Briki. Unraveling double stranded α-helical coiled coils: An X-ray diffraction study on hard α-keratin fibers. *Biopolymers*, 58(5):526–533, 2001.

[2] W. T. Astbury and A. Street. X-ray studies of the structure of hair, wool, and related fibres.- I. general. *Philosophical Transactions of the Royal Society of London. Series A, Containing Papers of a Mathematical or Physical Character*, 230(681-693):75–101, 1931.

[3] L. Kreplak, J. Doucet, P. Dumas, and F. Briki. New aspects of the α-helix to β-sheet transition in stretched hard α-keratin fibers. *Biophysical Journal*, 87(1):640–647, 2004.

[4] Jinan Cao. Is the α–β transition of keratin a transition of α-helices to β-pleated sheets. II. synchrotron investigation for stretched single specimens. *Journal of Molecular Structure*, 607(1):69–75, 2002.

[5] Kirill A Minin, Artem Zhmurov, Kenneth A Marx, Prashant K Purohit, and Valeri Barsegov. Dynamic transition from α-helices to β-sheets in polypeptide coiled-coil motifs. *Journal of the American Chemical Society*, 139(45):16168–16177, 2017.

[6] Donald J. Lyman, Jacqueline Murray-Wijelath, and Max Feughelman. Effect of temperature on the conformation of extended α-keratin. *Applied Spectroscopy*, 55(5):552–554, 2001.

[7] Yang Yu, Wen Yang, Bin Wang, and Marc André Meyers. Structure and mechanical behavior of human hair. *Materials Science and Engineering: C*, 73:152–163, 2017.

[8] Vesna Stanić, Jefferson Bettini, Fabiano Emmanuel Montoro, Aaron Stein, and Kenneth Evans-Lutterodt. Local structure of human hair spatially resolved by sub-micron X-ray beam. *Scientific Reports*, 5(1):17347–17347, 2015.

[9] Christopher Hammond. *The Basics of Crystallography and Diffraction*. IUCr texts on crystallography. Oxford University Press, Oxford, UK, 3rd edition, 2009.

[10] NASA's Goddard Space Flight Center. Electromagnetic spectrum. NASA Imagine the Universe. Available at `https://imagine.gsfc.nasa.gov/science/toolbox/emspectrum2.html` (Accessed: 2025-03-06).

[11] H. Schnablegger and Y. Singh. *The SAXS Guide: Getting Acquainted with the Principles*. Anton Paar GmbH, Graz, 5th edition, 2023.

[12] incoatec GmbH. Incoatec - innovative coating technologies, 2024. (Accessed: 2025-01-29).

[13] David Harvey. Instrument components in atomic X-ray spectrometry. `https://chem.libretexts.org/Bookshelves/Analytical_Chemistry/Instrumental_Analysis_%28LibreTexts%29/12%3A_Atomic_X-Ray_Spectrometry/12.02%3A_Instrument_Components`. Licensed under CC BY-NC-SA 4.0, (Accessed: 2025-03-06).

[14] Charles Kittel. *Introduction to Solid State Physics*. John Wiley & Sons, Hoboken, NJ, 8th edition, 2004.

[15] Rudolf Gross and Achim Marx. *Festkörperphysik*. Oldenbourg Wissenschaftsverlag, München, 2012.

[16] M. Ermrich, F. Hahn, and E. R. Wölfel. Use of imaging plates in X-ray analysis. *Textures and Microstructures*, 29:89–101, 1997.

[17] Fei Chi Yang, Yuchen Zhang, and Maikel C. Rheinstädter. The structure of people's hair. *PeerJ*, 2:e619, 2014.

[18] Sarthak Saha, Muhammad Arshad, Muhammad Zubair, and Aman Ullah. *Keratin as a Biopolymer*, pages 163–185. Springer International Publishing, Cham, 2019.

[19] David L. Nelson and Michael M. Cox. *Lehninger Principles of Biochemistry*. W. H. Freeman, New York, 6th edition, 2013.

[20] Alexander Müllner, Ruben Pahl, Doris Brandhuber, and Herwig Peterlik. Porosity at different structural levels in human and yak belly hair and its effect on hair dyeing. *Molecules*, 25(9):2143, 2020.

[21] ProUmid GmbH. Kontrollierte luftfeuchte mhg32, 2025. (Accessed: 2025-02-27).

[22] A. P. Hammersley. FIT2D: An introduction and overview, 1997. ESRF Internal Report ESRF97HA02T.

[23] Wolfram Research. *EstimatedBackground*, 2024. Wolfram Language function.

[24] Jinan Cao. Is the α–β transition of keratin a transition of α-helices to β-pleated sheets? part i. in situ XRD studies. *Journal of Molecular Structure*, 553(1-3):101–107, 2000.

List of Figures

A. Appendix

The following Python source code shows the program that was used to correct the issue of the spectra being shifted in q with respect to each other. This problem is described in the section 4.3.1 and illustrated in figure 4.3a. The program uses multiple Python packages such as `glob` and `os` for file handling, NumPy for numerical calculations as well as storing the data in arrays, `subprocess` to interact with an external program for plotting and various SciPy methods for the fitting data.

The usage of Gnuplot over, e.g., Matplotlib has some advantages. First of all, the Gnuplot window has a built-in data point cursor, allowing the user to read the coordinates of a specific point in the plot, by hovering over it with the cursor. The second advantage is that the Gnuplot window can refresh itself automatically, which makes processing multiple files easier. This means that one no longer has to close the plot window manually after each individual spectrum.[1]

The program itself is built to handle the integrated .chi files of the measurements. The user is asked for input of the path to the folder containing the data as well as a pattern, indicating the file type and a naming pattern to filter only certain files. The processed files will be saved in a new folder within the input folder. The program supports multiple fitting methods (Gaussian, split Gaussian, skew Gaussian, log-normal and gamma distribution), which the user can specify. With Gnuplot each spectrum is plotted individually and a user input for the q-coordinate of the Kapton peak is asked. Within an intervall of $\pm 0.3\ \mathrm{nm}^{-1}$ it then fits the peak and calculates the shift of the fitted peak center relative to a defined reference position (in this case $q_{reference} = 13.7\,\mathrm{nm}^{-1}$). In the next step all of the q-values of the spectrum are shifted by adding the calculated shift value. The processed spectrum is then saved in the output folder as a new .chi file.

```
# import of required packages
import numpy as np
import glob
import os
import subprocess
from scipy.optimize import curve_fit
```

[1] This is especially the case when running the program in Visual Studio Code.

```
from scipy.stats import skewnorm
from scipy.stats import gamma as gammaDist

# Definitions of the fitting functions
def gaussian(x, a, x0, sigma):
    return a * np.exp(-(x - x0)**2 / (2 * sigma**2))

def splitgauss(x, centre, sigma, sigma2):
    def unnnormgauss(x, centre, sigma):
        return np.exp(-(x-centre)**2/(2.*sigma**2))*np.sqrt(2/np.pi)
    return np.where(x < centre, unnnormgauss(x, centre, sigma),
    unnnormgauss(x, centre, sigma2))/(sigma+sigma2)

def skewGauss(x, centre, sigma, skew):
    return skewnorm.pdf(x, a=skew, loc=centre, scale=sigma)

def logNormal(x, centre, skew, **kwargs):
    " log Normal"
    return np.exp(-(((np.log(x)-centre)/skew)**2/2.0))/(x*skew*np.sqrt(np
    .pi*2.0))

def gammaDistribution(x, centre, sigma, a, **kwargs):
    "Gamma distribution"
    return gammaDist.pdf(x*centre, a, scale=sigma)

# plotting with gnuplot
def start_gnuplot():
    return subprocess.Popen(["gnuplot"], stdin=subprocess.PIPE, text=True
    )

def plot_with_gnuplot(gnuplot_process, x_values, y_values, file_name):
    gnuplot_script = f"""
    reset
    set title "Spectrum of {file_name}"
    set xlabel "q (1/nm)"
    set ylabel "Intensity"
    plot "-" using 1:2 with lines title "Original Spectrum"
    """

    gnuplot_process.stdin.write(gnuplot_script + "\n")

    for x, y in zip(x_values, y_values):
        gnuplot_process.stdin.write(f"{x} {y}\n")

```

```
48      gnuplot_process.stdin.write("e\n")
49      gnuplot_process.stdin.flush()
50
51  # choice of fitting methode
52  def fit_peak(x_values, y_values, mode):
53      if mode == "gaussian":
54          popt, _ = curve_fit(gaussian, x_values, y_values, p0=[max(
        y_values), x_values[np.argmax(y_values)], 0.1])
55          return popt[1]  # Return fitted peak position
56      elif mode == "splitgauss":
57          popt, _ = curve_fit(splitgauss, x_values, y_values, p0=[x_values[
        np.argmax(y_values)], 0.1, 0.1])
58          return popt[0]  # Return fitted centre
59      elif mode == "skewgauss":
60          popt, _ = curve_fit(skewGauss, x_values, y_values, p0=[x_values[
        np.argmax(y_values)], 0.1, 0.1])
61          return popt[0]  # Return fitted centre
62      elif mode == "lognormal":
63          popt, _ = curve_fit(logNormal, x_values, y_values, p0=[x_values[
        np.argmax(y_values)], 0.1])
64          return popt[0]  # Return fitted centre
65      elif mode == "gamma":
66          popt, _ = curve_fit(gammaDistribution, x_values, y_values, p0=[
        x_values[np.argmax(y_values)], 0.1, 1.0])
67          return popt[0]  # Return fitted centre
68      else:
69          raise ValueError("Invalid mode. Choose from 'gaussian', '
        splitgauss', 'skewgauss', 'lognormal', or 'gamma'.")
70
71  # reads in data values of the .chi files and stores it in an array
72  def read_chi_file(file_path):
73      data = []
74      header_lines = []
75      with open(file_path, "r") as file:
76          for line in file:
77              if line.strip() and not line.startswith("#"):
78                  try:
79                      x, y = map(float, line.split())
80                      data.append((x, y))
81                  except ValueError:
82                      continue
83              else:
84                  header_lines.append(line)
85      return np.array(data), header_lines
```

```
86
87 # writes the new corrected .chi files in the output folder
88 def write_chi_file(file_path, data, header_lines):
89     with open(file_path, "w") as file:
90         for line in header_lines:
91             file.write(line)
92         for x, y in data:
93             file.write(f"{x:.8E} {y:.8E}\n")
94
95 # searches for input data and creates output data
96 def align_chi_files(input_folder, pattern, mode="gaussian"):
97     files = glob.glob(os.path.join(input_folder, pattern))
98     if not files:
99         print("No matching files found.")
100        return
101
102    output_folder = os.path.join(input_folder, "shifted_files_fit")     #
       OUTPUT FOLDER NAME
103    os.makedirs(output_folder, exist_ok=True)
104
105    gnuplot_process = start_gnuplot()
106
107    for file in files:
108        print(f"Processing: {file}")
109
110        data, header_lines = read_chi_file(file)
111        x_values, y_values = data[:, 0], data[:, 1]
112
113        mask = (x_values >= 12) & (x_values <= 16)
114        x_plot, y_plot = x_values[mask], y_values[mask]
115        plot_with_gnuplot(gnuplot_process, x_plot, y_plot, file)
116
117        try:
118            start_guess = float(input("Enter starting guess for peak
       position: "))
119        except ValueError:
120            print("Invalid input. Skipping file.")
121            continue
122
123        min_bound, max_bound = start_guess - 0.3, start_guess + 0.3
124        search_mask = (x_values >= min_bound) & (x_values <= max_bound)
125
126        if not np.any(search_mask):
127            print(f"No data points found in the range ({min_bound}, {
```

```
    max_bound}). Skipping.")
128             continue
129
130         x_fit, y_fit = x_values[search_mask], y_values[search_mask]
131
132         try:
133             fitted_peak_x = fit_peak(x_fit, y_fit, mode)
134         except RuntimeError:
135             print(f"Fit failed for {file}. Skipping.")
136             continue
137
138         shift = 13.7 - fitted_peak_x
139         print(f"Shifting {file} by {shift:.4f}")
140         shifted_x_values = x_values + shift
141
142         output_path = os.path.join(output_folder, os.path.basename(file))
143         write_chi_file(output_path, np.column_stack((shifted_x_values,
    y_values)), header_lines)
144         print(f"Shifted spectrum saved to {output_path}")
145
146     gnuplot_process.stdin.write("exit\n")
147     gnuplot_process.stdin.close()
148
149 if __name__ == "__main__":
150     pattern = "*_hori_*.chi"    # filters only the spectra of a specified
     orientation
151     input_folder = r"<path_to_your_data>"   # input data
152     mode = "splitgauss"     # Enter fitting mode (gaussian/splitgauss/
    skewgauss/lognorm/gamma)
153     align_chi_files(input_folder, pattern, mode)
```

Listing A.1: Python source code for the correction of the in q shifted files.